Soft Matter

Rotating Crystals of Magnetic Janus Colloids

Journal:	*Soft Matter*
Manuscript ID:	SM-ART-09-2014-001962.R1
Article Type:	Paper
Date Submitted by the Author:	02-Oct-2014
Complete List of Authors:	Yan, Jing; University of Illinois, Bae, Sung Chul; UNIST, Granick, Steve; 106 Materials Research Laboratory, Department of Chemistry

Soft Matter RSCPublishing

ARTICLE

Rotating Crystals of Magnetic Janus Colloids

Cite this: DOI: 10.1039/x0xx00000x

J. Yan,[a] S. C. Bae[b] and S. Granick[a]

Received 00th January 2012, Accepted 00th January 2012

DOI: 10.1039/x0xx00000x

www.rsc.org/

Monodisperse magnetic colloids are found to self-assemble into unusual crystals in the presence of rotating magnetic fields. First, we confirm a predicted phase transition (S. Jäger and S. H. L. Klapp, *Soft Matter* 2011, **7**, 6606-6616, Ref. 1), directly coupled to the dynamic transition of single particle motion, from disorder to hexagonal crystal. Next, going beyond what had been predicted, we report how hydrodynamic coupling produces shear melting, dislocations, and periodically mobile domain boundaries. These uniform magnetic colloids, whose structures are modulated *in situ* using the protocols described here, demonstrate a strategy of stimulus-response in the colloid domain with potential applications.

1 Introduction

The directed assembly of particulate matter by external fields is of mounting topical interest for potential applications in optics,[2] structural materials,[3] microfluidic devices,[4] sensors,[5] and robotics.[6] To accomplish this, magnetic control presents unique advantages as not only does its remote application simplify device integration but also, magnetic interaction is easy to model and characterize due to its unscreened nature in electrolyte solutions.[7] Static magnetic fields can direct isotropic magnetic particles into periodic lattices,[8] but a growing trend is to use time-dependent fields such as alternating,[9] biaxial,[10] and triaxial fields.[11] For example, colloidal membranes have been synthesized using a precessing (triaxial) field at the "magic" precession angle.[12] The resulting structures can have anisotropic magnetic, electrical, and thermal properties with potential applications in responsive materials which can be reconfigured upon external triggering.[3]

Most efforts to date involve the induced dipoles of paramagnetic and superparamagnetic spheres,[10,13-15] or magnetic holes in a paramagnetic solution.[16] Spheres of this kind do not move in space individually when they experience a time-varying magnetic field, because their magnetic moment follows the field instantaneously. The resulting self-assembled structures can then be understood by considering time-averaged interaction and equilibrium arguments only.[17] Even more interesting phenomena arise when particles possess permanent dipoles: these are ferromagnetic colloids. Then, time-varying fields act on entire particles, not simply on their magnetic moment. Consequently, such particles undergo physical motion and experience viscous resistance when they are suspended in liquid.[18,19] They are the objects of this study.

For the prototypical case of a circularly rotating field, Kopelman and coworkers studied extensively the dynamics of individual magnetic colloids,[20] showing that at low frequency they rotate synchronously with the field, while above a threshold frequency, viscous drag prevents them from frequency locking. Recently, Klapp and coworkers showed from computer simulation that the loss of synchronicity of single particle motion can produce a macroscopic phase transition from a layered to a disordered state.[1] More recently, the same group investigated the effect of hydrodynamic interaction arising from the rotation-translation coupling of such particles through the viscous medium.[21] To the best of our knowledge, these predictions did not see prior experimental test.

Here, to achieve homogeneous magnetic response, we use monodisperse spheres with magnetic coating on one side to be "Janus" and study the dynamic self-assembled structures of these magnetic particles in rotating magnetic fields. First, we observe a phase transition from disordered to an ordered hexagonal crystal, and conclude that the mechanism is coupled directly to a dynamical transition of single particle motion. Next, we observe that the hydrodynamic interaction between these particles, which for paramagnetic particles would be absent, results in intriguing phenomena not predicted by prior theory: shear melting at the edge, dislocation formation and rotation, and periodic dynamic pattern of domain boundaries.

2 Method

2.1 Particle Design and Synthesis

Magnetic Janus particles were selected as the experimental realization of dipolar spheres, as they are so experimentally convenient: they can be prepared in large quantity with very homogenous magnetic properties.[22,23] Meanwhile, the optical contrast of Janus spheres allows rotation to be visualized, while for isotropic spheres this cannot be done simply. The magnetic Janus particles were synthesized using directional electron beam deposition onto silica particles with diameter d = 2 μm (Tokuyama) or 1.6 μm (NIST), prepared as a two-dimensional submonolayer on a Piranha-treated glass slide (Figure 1a). We then sequentially coated nickel (typical thickness was 18 nm) and SiO_2 (typical thickness was 15 nm) onto one side of these spherical shapes.

The magnetic response of these Janus spheres has been reported in Reference 11. Briefly, the particles possess both ferromagnetic and paramagnetic responses, mainly in the direction parallel to the Janus interface.

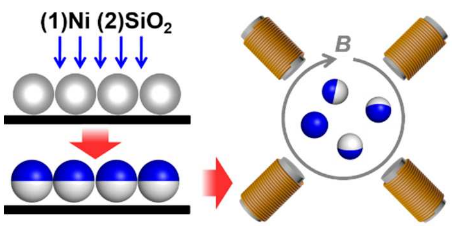

Figure 1. Experimental scheme. Thin coatings of first Ni and then protective SiO_2 are sequentially deposited onto the top side of micron-sized silica spheres to produce Janus particles. After release into water, the coated spheres are subjected to a rotating magnetic field provided by two orthogonal pairs of solenoid coils.

2.2 Assembly Protocol

After sonication to release the particles into deionized water, we further sonicated the particles for another 30 minutes to remove any residual aggregates. We then introduced the suspension into an optical imaging chamber (Lab-Tek II chambered cover glass). Placed in aqueous suspension, they sediment close to the chamber bottom but are levitated by electrostatic repulsion from the charged wall. We then applied a homogenous rotating magnetic field, typically at 20 Hz and strength up to 2 mT (Figure 1b). The rotating magnetic field was generated by applying two sinusoidal signals with a $\pi/2$ phase shift to two pairs of iron-core solenoids (Science Source) placed orthogonally, using a function generator (Agilent 33522A) coupled to a dual channel power amplifier (Crown, XLS 202). Movies were taken in a home-built microscope using an LED light source (Thorlabs MCWHL2), a 50× long-working-distance objective (Mitutoyo, N.A. = 0.55) and a CMOS camera (Edmund Optics 5012M GigE). The liquid-solid transition was mapped at constant frequency ω_B while slowly increasing the field strength B.

2.3 Image Analysis

Image analysis was performed with home-written Matlab code. Particle positions were tracked using the circle finding functions in the image analysis toolbox. To track rotation of the whole crystal, we applied a fast Fourier transform on the image and followed the motion of one of the six diffraction spots. To obtain particle trajectories, we developed a rotational version of correlated image tracking.[24] Particles were first assumed to rotate with respect to the crystal center at the same angular speed, and from this their locations in the next time frame were predicted. By comparing the predicted to the actual positions, we mapped the particle identity. Standard Delaunay triangulation was performed to obtain the number of nearest neighbours of a particle and to identify dislocation pairs.

2.4 Definition of Order Parameters

We followed the standard definition of order parameters for hexagonal crystals.[25,26] For each particle in a cluster, a local six-fold bond-orientational order parameter φ_6 is defined as:

$$\varphi_6(\vec{r}_j) = N_{\mathrm{nn}j}^{-1} \sum_{k=1}^{N_{\mathrm{nn}j}} e^{i6\theta_{jk}}$$

in which $N_{\mathrm{nn}j}$ is the number of nearest neighbours of particle j at position $\vec{r}_j$, and θ_{jk} is the angle between an arbitrary axis and the line connecting the centers of particles j and k. The positional order parameter s for particle j is defined as:

$$s(\vec{r}_j) = e^{i\vec{G}\cdot\vec{r}_j}$$

in which $\vec{G}$ is the reciprocal lattice vector of the hexagonal lattice. After calculating φ_6 and s for all particles in the cluster, a global bond-orientational order parameter Ψ_6 is defined as:

$$\psi_6 = N^{-1}\left|\sum_{j=1}^{N} \varphi_6(\vec{r}_j)\right|$$

The global positional order parameter S is similarly defined as:

$$S = N^{-1}\left|\sum_{j=1}^{N} s(\vec{r}_j)\right|$$

3 Results and Discussion

3.1 Liquid-to-Crystal Transition Coupled with Dynamic Transition of Individual Spheres

Interparticle attraction causes these particles to assemble into clusters when a rotating magnetic field is applied, and their internal order depends exquisitely on field strength. At low field strength, the cluster is liquid-like: it has no positional order (Figure 2a). Meanwhile, the Janus director, defined as the unit vector pointing from a particle's uncoated side to the coated side, has random orientation. The rotation of individual particles does not follow the field, but exhibits periodic backward-rocking characteristic of asynchronous rotation.[20]

Above a threshold field strength, the cluster becomes an ordered hexagonal crystal (Figure 2b, Supplementary Movie 1) in which the Janus directors point perpendicular to the image. Experimentally, this shows up as the visual appearance of opaqueness. Close inspection shows that individual particles continue to rotate with the frequency of the magnetic field (ω_B) while the self-assembled crystal also rotates but more slowly, suggesting that the liquid-to-crystal transition might stem from a transition in single-particle dynamics. To understand this, consider that a rotating magnetic field exerts a torque on a dipole $\tau_{\mathrm{mag}} = \vec{m}_0 \times \vec{B} = m_0 B \sin\varphi$, where m_0 is the dipole moment and $\varphi = \omega_B t - \theta$ is the phase lag of the dipole with the external field.[23] $\vec{B}$ stands for the time-varying magnetic field and θ is the instantaneous phase of the magnetic dipole. The rotating particle also experiences a viscous torque $\tau_{vis} = \pi\eta d^3 d\varphi/dt$, in which η is the solvent viscosity. Neglecting inertia in this low Reynolds number situation, one balances the two torques and concludes that $d\varphi/dt = \omega_B/\omega_c - \sin\varphi$, in which the critical frequency is $\omega_c = m_0 B/\pi\eta d^3$. For $\omega_B < \omega_c$, the solution to this equation is $d\varphi/dt = 0$, signifying that the particle rotates synchronously with the field, with the same speed and a constant phase lag. But for $\omega_B > \omega_c$, no steady solution exists.

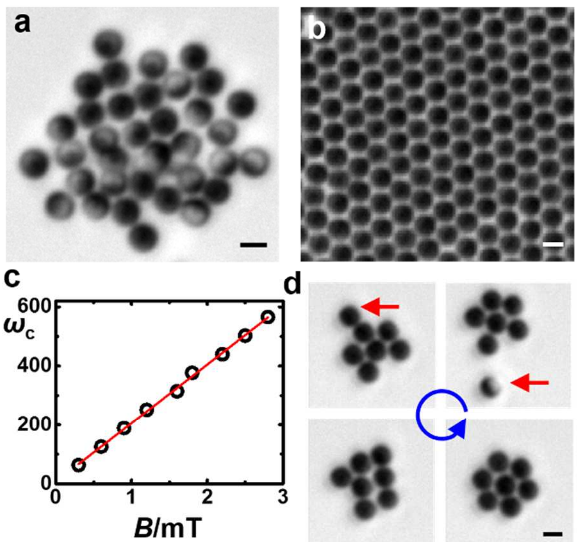

Figure 2. Liquid-crystal transition. (a) Image of a disordered cluster that formed in an 0.6 mT, 20 Hz rotating magnetic field. (b) Image within a hexagonal crystal that formed in a 1.0 mT, 20 Hz rotating magnetic field. (c) Critical frequency ω_c (units: rad/s) plotted against field strength B. The red line is a linear fit. (d) Images showing the kinetic formation of a hexagon. Note the orientation change of the particle being incorporated, indicated by red arrows. Times are t = 0, 0.59, 0.66, 1.75 s, counterclockwise from the top right. Scale bar is 2 μm.

Experimentally, we mapped the relation between the critical frequency ω_c and field strength B (Figure 2c) by visually detecting the transition from liquid to hexagonal state, and observed a clean linear relation from whose slope we inferred m_0 to be 5.0×10^{-15} A·m^2, in pleasing agreement with the value estimated independently from the hysteresis curve.[11] This provides experimental confirmation that the dynamic transition of individual particles dictates structural change of the assembled cluster – confirming a prediction of simulation.[1]

Several items merit discussion regarding particle rotation inside this moving crystal. First, in addition to the remnant magnetic moment on which our analysis up to this point was based, it is true that these particles also possess strong paramagnetic response, visible in the magnetic hysteresis curves.[11] Recently, this laboratory worked out the equation of motion of such particles in a precessing magnetic field by modeling them as purely paramagnetic particles.[11] A precession angle of 90° is equivalent to a rotating field of concern here. However, solving the equation for this value of precession angle leads to singularity solution, such that individual spheres rotate with their Janus director always pointing perpendicular to the rotating field. This is not what we observed for isolated spheres (see below). Meanwhile, the scaling relationship of $\omega_B \propto B$ is also inconsistent with the prediction for paramagnetic particles. It seems that the dynamics of magnetic Janus spheres is governed by the residual dipolar moment, not by the paramagnetic component of the response, in this particular case of a purely rotating magnetic field.

Second, it is intriguing that in a cluster all particles point their magnetic cap perpendicular to the rotating field, as the equation of motion places no restriction on the Janus director's orientation. The most likely cause is optimization of interparticle dipole-dipole interaction. In such particles, the location of the dipole is shifted from the geometric center due to the asymmetric coating,[27,28] causing the dipole-dipole distance between neighbouring particles to depend not only on the relative position but also on orientation. The observed configuration equalizes all dipole-dipole separations, thus minimizing the total magnetic energy. Supporting this hypothesis is the change of state when a particle becomes incorporated into a cluster (Figure 2d, Supplementary Movie 2). In this movie, one sees that although particles do possess freedom of orientation when isolated, they adopt a "full moon" configuration once inside a cluster. In contrast, in the liquid state, this orientation locking is lost. Parenthetically, there is no magnetic energy difference between the up and down configurations for a single sphere, but gravitational energy encourages the metal-coated hemisphere to point down due to the extra weight of the coating. For these reasons, we expect all particles in a cluster to point down towards the substrate in principle,

Third, while hexagonal order in the observed rotating crystalline state is more pronounced than in the simulations,[1] this is simply because the experiments concern larger particles, hence less thermal motion. There is essential agreement that an isotropic, time-averaged interaction, balanced here by electrostatic repulsion, creates a potential that leads naturally to hexagonal packing. The detailed form and characterization of the potential is reported in Reference 29.

3.2 Cluster Rotation

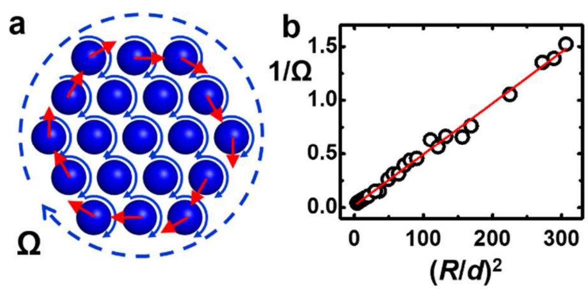

Figure 3. Crystal rotation. (a) Schematic representation of the rotation mechanism. Particles at the edge experience an unbalanced hydrodynamic shear force tangent to the edge (circle of red arrows). (b) Inverse angular velocity 1/Ω plotted as a function of $(R/d)^2$, where R is the size of the crystal piece and d = 1.6 μm is particle diameter in order to access large crystal size. Red line is a linear fit.

Next, we consider rotation of the entire crystalline cluster. The following argument can explain this rotation and predict the scaling between the crystal size R and the rotation speed Ω (Figure 3a). First, notice that a fast-spinning sphere with angular speed ω creates a flow field and exerts shear force F_{shear} on a nearby particle with the same motion $F_{shear} = 0.2\pi\eta\omega d^2 \ln(H/d)$,[30] in which H is the surface-to-surface separation between the particles. This is valid in the limit $H << d$, which applies here on physical grounds. This force provides the torque to rotate a pair of particles at a frequency $\Omega = 0.13\ln(d/H)\omega$.[31] From image analysis, we estimated H to be 200-400 nm, corresponding to Ω = 0.2-0.3ω for a pair of spheres, close to the experimental observation.

Now extend this analysis to the entire crystalline cluster, considering just the force from nearest neighbours to first approximation, which makes sense since the forces are short-ranged. For particles in the interior of a crystal, the total shear force vanishes by symmetry. Only those at the edge experience an unbalanced force tangent to the interface (Figure 3a). In other words, the cluster experiences an effective shear applied at its edge and hence the cluster rotates.[32] Then, in the continuum approximation, the shear torque scales with both the number of particles at the edge ($\propto 2\pi R$) and the cluster diameter, hence scales as R^2, while the viscous drag of this rotating disk scales as ΩR^4, so that the balance of these two torques gives $\Omega \propto R^{-2}$. Measurements are consistent with this hypothesis (Figure 3b).

3.3 Shear Melting

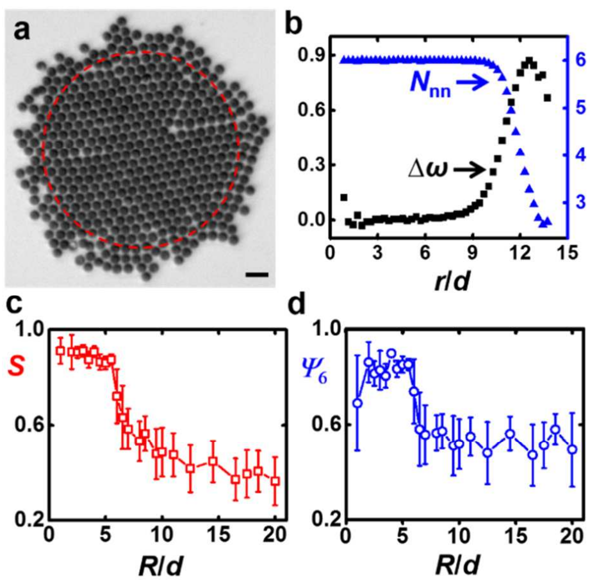

Figure 4. Shear melting. (a) Image of a crystal with shear-melted edge. The dotted red circle delineates the boundary between solid and shear-melted region. Scale bar is 5 μm. (b) Plotted against the distance r from a cluster's center, the abscissa shows the average number of nearest neighbours N_{nn}. (c-d) Positional order parameter S and bond-orientational order parameter Ψ_6 as a function of cluster size R (analysed with 1.6 μm spheres).

Experiments confirm the edge shear melting that can be expected from the edge-shearing mechanism. Figure 4a shows that in a larger cluster, particles close to the center remain hexagonally ordered and undergo rigid body rotation, while near the edge particles rotate more rapidly (with respect to the cluster center) because of stronger shear. This is a sharp transition: Figure 4b plots the local angular velocity $\Delta\omega$ and number of nearest neighbours (N_{nn}) as a function of radial distance from the cluster center r. Once the particles at the edge are driven out of their equilibrium lattice position, they experience an unbalanced shear force that causes them to move faster than particles within the intact lattice, which can be clearly seen in Supplementary Movie 3. The interfacial width of several particle diameters is an interesting effect not yet modeled to the best of our knowledge. Experimentally, we observed an almost constant boundary layer thickness of about $3d$, regardless of the overall cluster size if the magnetic field strength and frequency were kept the same.

To quantify the shear melting transition, we tracked the positional order parameter S and the bond-orientational order parameter Ψ_6 (see Method session for definition) as a function of cluster size R (Figure 4c-d). Indeed, above a critical radius about $6d$, both order parameters experience a sharp drop, indicating the formation of the disordered boundary layer. This appears to be the point at which shear force at the edge dominates over rigidity of the crystal: the edge is shear-melted.[33]

3.4 Dislocation Dynamics

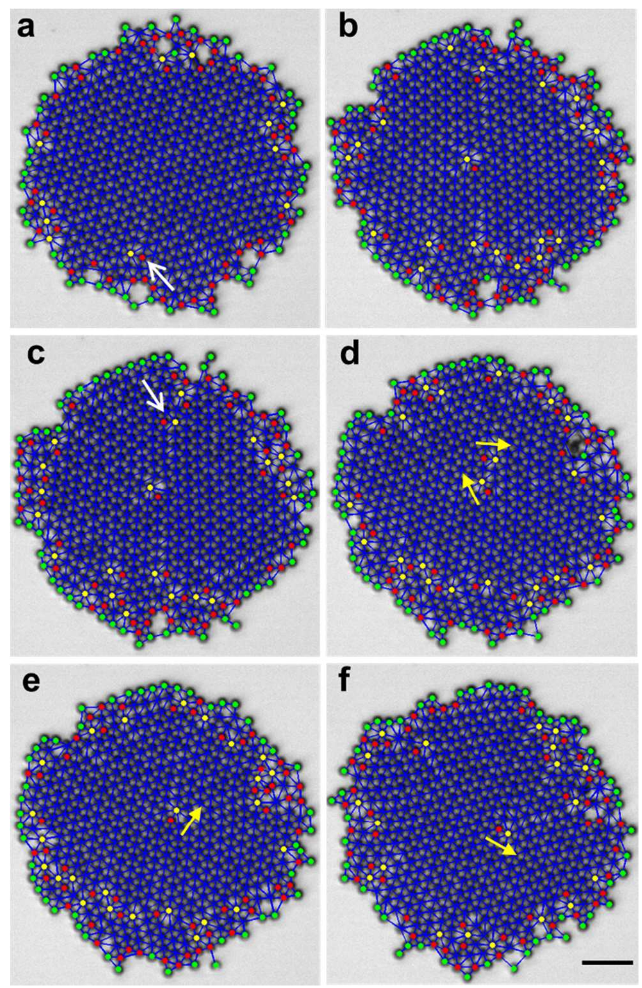

Figure 5. Dislocation dynamics. (a-f) Images at times t = 0, 0.76, 0.81, 0.89, 0.91, 1.04 s, respectively. Red, yellow, and green dots represent particles with N_{nn} = 5, 7, and < 5, respectively. A red dot and a yellow dot form a dislocation with 5-7 dipole orientation indicated by the yellow arrows. White arrows indicate newborn free dislocations. Scale bar is 10 μm.

The disordered boundary at the edge provides a continuous source of defects, the most common ones being dislocations (Supplementary Movie 4).[34] Dislocations are readily identified as a pair of particles with number of nearest neighbours $N_{nn} = 5$ and 7 (Figure 5),[35] and are initiated by dissociation of dislocation pairs.[36] Free dislocations have the 5-7 dipole direction preferentially oriented tangent to the edge. Once the dislocations detach from the edge, we observed that they tend to move towards the cluster center in a gliding motion (Figure 5a-b). Furthermore, after one free dislocation reaches the cluster center, a new free dislocation emerges at the cluster edge, oriented at an angle 120° (Figure 5c). The newborn dislocation quickly travels towards the center (Figure 5d) and merges with the first one, producing a new dislocation with direction determined by vector addition (Figure 5e). This mechanism repeats regularly. It gives the central dislocation a discrete, apparent rotation in the reference frame of the rotating crystal (Figure 5d-f).

Physically, we imagine the mechanism to be that particles at the exterior experience larger viscous drag because of their larger linear velocity, which creates stress in the crystalline core. Formation of dislocations releases this stress to some extent, even though it comes at the cost of additional elastic energy.[37] Since the energy associated with stress scales with R more strongly than does the dislocation energy, this explains why crystals above a critical size spontaneously release stress by forming dislocations. Meanwhile, this might explain our observation of a constant boundary layer thickness: the cluster self-regulates the edge shear stress by either causing the boundary spheres to move, or by generating defects in the crystalline core. It will be interesting in the future to build theoretical models for this self-regulation mechanism. Once formed, a dislocation with its Burger's vector in the radial direction experiences a Peach-Kohler force that drives it towards the center, where shear stress vanishes.[38]

3.5 Grain Boundary Dynamics

In even larger crystals, dislocations connect to form grain boundaries; this splits the crystal into multiple domains. Again, quasi-periodic behavior is observed (Supplementary Movie 5): first a single crystal builds up stress, which then is released by breaking into multiple domains separated by clear domain boundaries (Figure 6a), but domain boundaries heal over time to reestablish a uniform crystalline core (Figure 6b), and this pattern repeats. Tracking the time dependence of total number of dislocations N in the solid core (Figure 6c) reveals occasional bursts and sudden decrease of N, which quantifies the scenario just described.

Imaging a smaller cluster allows one to see more directly the mechanism of periodic healing with assistance from analysis using Delaunay triangulation (Figure 6d-g and Supplementary Movie 6). One sees that the grain boundary is easily identified as a string of dislocations. Starting from a strained single crystal, a small part of the crystal begins to adopt a crystal orientation different from the bulk, assisted by its dislocations. With time, the mismatch grows and develops into a separate microdomain that rotates not only around the center of the entire cluster but also around its own center. But when the phase of the small domain exceeds that of the large domain by the angular period of a hexagonal lattice (60°), the two domains regain registry. Hence, we attribute the observed pattern of bursts and decrease in N to the periodic release of strain into grain boundaries and the subsequent, differential rotation of domains of different mass, which restores crystallinity.

The periodic formation and reunion of multiple domains also explains the different behavior of the two order parameters S and Ψ_6 for large clusters (Figures 4c-d). S characterizes global positional order and hence is more sensitive to defects and polycrystallinity. Thus, S keeps declining as cluster size grows and multiple domains form. In contrast, Ψ_6 is a more local measurement of order; it stays flat for larger R as long as the cluster keeps a hexagonally ordered core. Both S and Ψ_6 show large temporal fluctuations even for a single cluster (reflected by the large error bars), as domains periodically break and reunite.

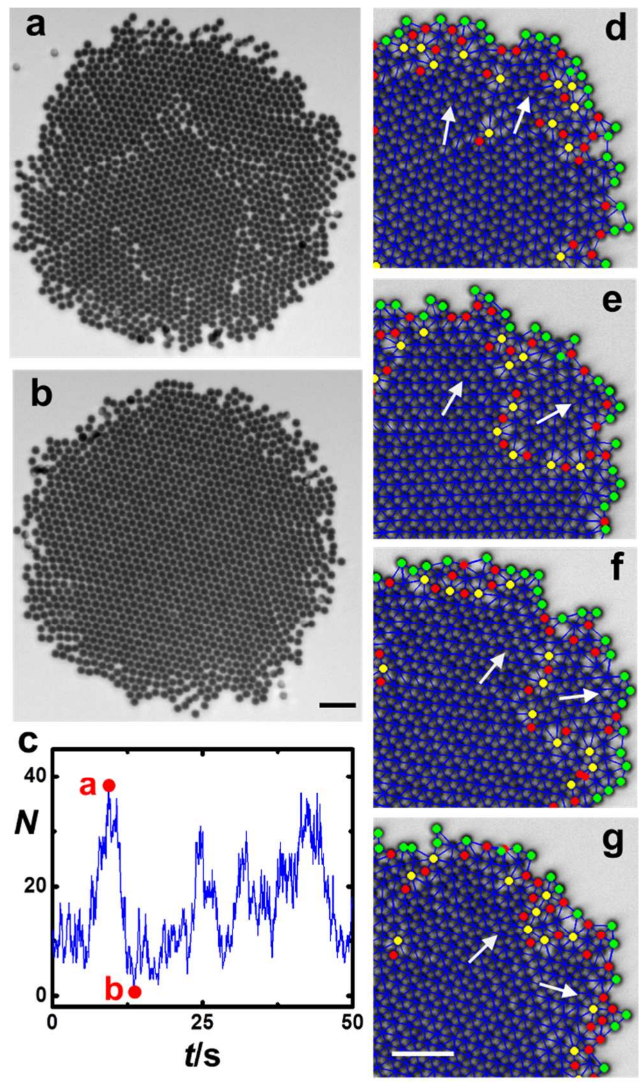

Figure 6. Grain boundary dynamics. (a,b) Images of a large cluster undergoing periodic breakdown into multiple domains followed by reunion into a single crystal at times t = 9.4 and 13.6 s, respectively. (c) The number of dislocation pairs N within the crystalline core is plotted against time for the sample illustrated in panels a-b. (d-g) Images showing a cycle of domain dynamics. White arrows show crystal orientation of the majority and minority domains. The time interval is 0.36 s between (d) and (e) and 0.15 s in (e-g). Scale bar is 10 μm.

4. Conclusions

In this study, we experimentally report the predicted "layering transition" of particles with magnetic dipoles in a rotating magnetic field. To the best of our knowledge, it is the first such report. We confirm that this structural transition is dictated by a dynamic transition on a single particle level, from synchronous to asynchronous rotation. This physical system contrasts with the much-studied alternative system of paramagnetic particles, for which particle motion is decoupled from the magnetic moment, and hence for which single particle dynamics is not relevant. Going beyond confirmation of what had already been predicted, we have demonstrated a plethora of dynamic patterns: edge shear melting, dislocation generation and recombination, and periodic domain dynamics, all arising from hydrodynamic interactions between rotating spheres that can be understood from simple scaling arguments. The same physical ideas may extend to the behavior of nanocrystals under mechanical shear,[39] whose lattice distortions are interesting yet difficult to measure at the atomic level, but are described here from direct experiment using particles that are large enough to image *in situ* optically. Meanwhile, we also envision that the current methodology can be applied to the directed self-assembly of magnetic nanoparticles.[2] Although they are one or two orders of magnitude smaller than the particles used in the current study, they can be made of pure magnetic materials rather than a thin shell and hence have sufficiently strong attraction to balance thermal randomization.

Rotating fields represent the simplest time-dependent field. Extension to multiaxial fields is anticipated to generate more interesting dynamics, not only on the single particle level but also on larger scales. Regarding the magnetic particles themselves, extending spheres studied here to anisotropic shapes should bring another dimension into the problem, in the future.[40,41] The interplay between the dipolar interactions and anisotropic shape should give rise to crystals with new symmetries.[42,43] The directional coating method used in this study is compatible with the rapidly expanding repertoire of colloids with nonspherical shapes, as methods are known how to introduce magnetic coatings onto them afterwards.[44] New interesting physics and applications should be anticipated.

Acknowledgements

We thank Gregory Grason and Amir Azadi for discussions. This work was supported by the U.S. Department of Energy, Division of Materials Science, under Award No. DE-FG02-07ER46471 through the Frederick Seitz Materials Research Laboratory at the University of Illinois at Urbana-Champaign.

Notes and references

[a] Departments of Materials Science and Engineering, Chemistry and Physics, University of Illinois at Urbana-Champaign
1304 W. Green St., Urbana, IL 61801, United States
[b] Department of Biomedical Engineering
Ulsan National Institute of Science and Technology
UNIST-gil 50, Ulju-gun, Ulsan, 689-798, Korea

Electronic Supplementary Information (ESI) available: Supplementary Movies 1-6 are available. See DOI: 10.1039/b000000x/

1. S. Jäger and S. H. L. Klapp, *Soft Matter*, 2011, **7**, 6606-6616.
2. M. Wang, L. He and Y. Yin, *Mater. Today*, 2013, **16**, 110-116.
3. J. E. Martin, *Composites Part. A*, 2005, **36**, 545-548.
4. P. S. Doyle, J. Bibette, A. Bancaud and J. L. Viovy, *Science*, 2002, **295**, 2237-2237.
5. D. H. Read and J. E. Martin, *Adv. Funct. Mater.*, 2010, **20**, 1577-1584.
6. J. Kim, S. E. Chung, S.-E. Choi, H. Lee, J. Kim and S. Kwon, *Nat. Mater.*, 2011, **10**, 747-752.
7. P. Tierno, *Phys. Chem. Chem. Phys.*, 2014.
8. A. P. Hynninen and M. Dijkstra, *Phys. Rev. Lett.*, 2005, **94**, 138303.
9. J. W. Swan, J. L. Bauer, Y. Liu and E. M. Furst, *Soft Matter*, 2014, **10**, 1102-1109.
10. D. Du, D. Li, M. Thakur and S. L. Biswal, *Soft Matter*, 2013, **9**, 6867-6875.
11. J. Yan, M. Bloom, S. C. Bae, E. Luijten and S. Granick, *Nature*, 2012, **491**, 578-581.
12. N. Osterman, I. Poberaj, J. Dobnikar, D. Frenkel, P. Ziherl and D. Babić, *Phys. Rev. Lett.*, 2009, **103**, 228301.
13. J. Dobnikar, A. Snezhko and A. Yethiraj, *Soft Matter*, 2013, **9**, 3693-3704.
14. P. Tierno, R. Muruganathan and T. M. Fischer, *Phys. Rev. Lett.*, 2007, **98**, 028301.
15. A. Weddemann, F. Wittbracht, B. Eickenberg and A. Hütten, *Langmuir*, 2010, **26**, 19225-19229.
16. J. Černák and G. Helgesen, *Phys. Rev. E*, 2008, **78**, 061401.
17. N. Casic, S. Schreiber, P. Tierno, W. Zimmermann and T. M. Fischer, *Euro. Phys. Lett.*, 2010, **90**, 58001.
18. B. A. Grzybowski, H. A. Stone and G. M. Whitesides, *Nature*, 2000, **405**, 1033-1036.
19. G. Kokot, A. Snezhko and I. S. Aranson, *Soft Matter*, 2013, **9**, 6757-6760.
20. B. H. McNaughton, K. A. Kehbein, J. N. Anker and R. Kopelman, *J. Phys. Chem. B*, 2006, **110**, 18958-18964.
21. S. Jäger, H. Stark and S. H. L. Klapp, *J. Phys.: Condens. Matter*, 2013, **25**, 195104.
22. A. Walther and A. H. E. Müller, *Soft Matter*, 2008, **4**, 663-668.
23. I. Sinn, P. Kinnunen, S. N. Pei, R. Clarke, B. H. McNaughton and R. Kopelman, *Appl. Phys. Lett.*, 2011, **98**, 024101.
24. R. Besseling, L. Isa, E. R. Weeks and W. C. K. Poon, *Adv. Colloid Interface Sci.*, 2009, **146**, 1-17.
25. K. Zhao and T. G. Mason, *Phys. Rev. Lett.*, 2009, **103**, 208302.
26. K. J. Strandburg, *Rev. Mod. Phys.*, 1988, **60**, 161-207.
27. M. Klinkigt, R. Weeber, S. Kantorovich and C. Holm, *Soft Matter*, 2013, **9**, 3535-3546.
28. A. I. Abrikosov, S. Sacanna, A. P. Philipse and P. Linse, *Soft Matter*, 2013, **9**, 8904-8913.
29. J. Yan, S. C. Bae, S. Granick, *Adv. Mater.*, submitted.
30. A. J. Goldman, R. G. Cox and H. Brenner, *Chem. Eng. Sci.*, 1967, **22**, 637-651.
31. K. Drescher, K. C. Leptos, I. Tuval, T. Ishikawa, T. J. Pedley and R. E. Goldstein, *Phys. Rev. Lett.*, 2009, **102**, 168101.

32. J. Schwarz-Linek, C. Valeriani, A. Cacciuto, M. E. Cates, D. Marenduzzo, A. N. Morozov and W. C. K. Poon, *Proc. Natl. Acad. Sci.*, 2012, **109**, 4052-4057.
33. Y. L. Wu, D. Derks, A. van Blaaderen and A. Imhof, *Proc. Natl. Acad. Sci.*, 2009, **106**, 10564-10569.
34. D. R. Nelson, *Defects and Geometry in Condensed Matter Physics*, Cambridge University Press, Cambridge, England, 2001.
35. W. T. M. Irvine, M. J. Bowick and P. M. Chaikin, *Nat. Mater.*, 2012, **11**, 948-951.
36. V. Nosenko, G. E. Morfill and P. Rosakis, *Phys. Rev. Lett.*, 2011, **106**, 155002.
37. G. M. Grason, *Phys. Rev. Lett.*, 2010, **105**, 045502.
38. A. Azadi and G. M. Grason, *Phys. Rev. E*, 2012, **85**, 031604.
39. J. R. Greer and J. T. M. De Hosson, *Prog. Mater. Sci.*, 2011, **56**, 654-724.
40. S. Sacanna, D. J. Pine and G.-R. Yi, *Soft Matter*, 2013, **9**, 8096-8106.
41. R. M. Erb, J. Segmehl, M. Charilaou, J. F. Loffler and A. R. Studart, *Soft Matter*, 2012, **8**, 7604-7609.
42. S. Kantorovich, E. Pyanzina and F. Sciortino, *Soft Matter*, 2013, **9**, 6594-6603.
43. S. C. Glotzer and M. J. Solomon, *Nat. Mater.*, 2007, **6**, 557-562.
44. J. Yan, K. Chaudhary, S. C. Bae, J. A. Lewis and S. Granick, *Nat. Commun.*, 2013, **4**, 1516-1516.

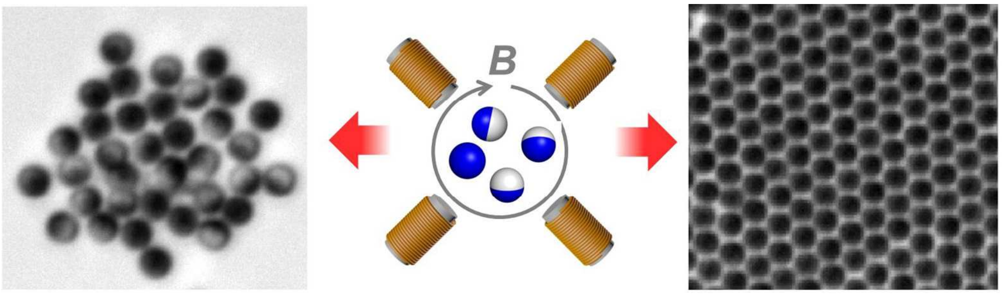

Shear melting, dislocations, and periodically mobile domain boundaries are observed in rotating magnetic crystals
279x80mm (150 x 150 DPI)